# Journal of Materials Chemistry A

Accepted Manuscript


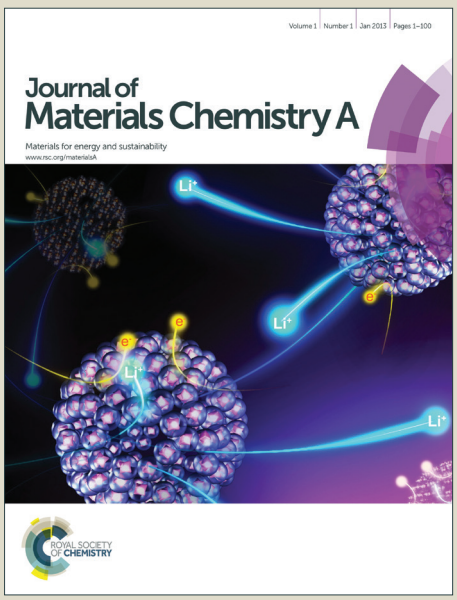





ROYAL SOCIETY OF CHEMISTRY

www.rsc.org/materialsA

Journal Name

RSCPublishing

ARTICLE

Cite this: DOI: 10.1039/xoxxoooooox

# Nanocomposites based on Hofmann-type structure $Ni^{II}(pz)[Ni^{II}(CN)_4]$ (pz = pyrazine) nanoparticles for reversible iodine capture.

Received ooth January 2012,
Accepted ooth January 2012

DOI: 10.1039/xoxxoooooox

www.rsc.org/

G. Massasso,[a] M. Rodriguez-Castillo,[a] J. Long,[a] A. Grandjean,[b] B. Onida,[c] Y. Guari,[a*] Ch. Guerin[a] and J. Larionova[a]

Hybrid nanocomposites based on nanoparticles of the Hofmann-type structure $Ni^{II}(pz)[Ni^{II}(CN)_4]$ (where pz = pyrazine) confined into mesoporous silica or porous glass pearls were synthesised by sequential coordination of the molecular precursors into the pores of the functionalized matrices. Infrared (IR) and UV/Visible (UV-Vis) spectroscopies, powder X-Ray diffraction (PXRD), Transmission Electron Microscopy (TEM) analyses reveal the presence of uniformly-sized spherical $Ni^{II}(pz)[Ni^{II}(CN)_4]$ nanoparticles of 3-6 nm, which are homogeneously dispersed into the matrices. These nanocomposites are able to efficiently capture iodine from cyclohexane solutions with a maximal sorption capacity of 1.75 mmol per g of materials. A particular emphasis is given on the mechanism of iodine sorption as well as on the sorption cycling ability of materials.

## Introduction

Radioactive iodine isotopes produced during the fission of $^{235}U$ and, particularly the **γ**-rays emitter $^{129}I$ having a long half-life ($1.57 \cdot 10^7$ years), are dangerous for health due to their volatility, toxicity and their persistence in the environment.[1] Nuclear industry attaches a great deal of attention to their efficient and selective capture during fuel reprocessing or in case of off-normal working conditions in order to minimize their environmental impact. Several processes for iodine treatment in its elemental and diatomic ($I_2$) form are currently used in reprocessing plants. They consist in: (*i*) scrubbing with an alkaline solution and precipitation of stable and insoluble compounds, like NaI and $NaIO_3$; (*ii*) the "Mercurex" process, which uses a mercuric nitrate-nitric acid solution to precipitate $HgI_2$; or (*iii*) the "Iodox" process employing hyperazeotropic nitric acid scrub solution to solubilize and oxidize iodine to $(IO_3)^-$ species with their further precipitation and encapsulation as $Ba(IO_3)$.[2, 3] These methods present various unattractive features such as multi-steps technology, indirect iodine treatment in liquid phases, corrosiveness, potential formation of nitrated organics, and an important volume of radioactive wastes, which should be then retreated. Recently, direct gas phase iodine trapping by using silver-impregnated zeolites with formation of insoluble and stable AgI was also applied in industry. But this process is relatively expensive and presents a limited weight capacity of 33 %.[4, 5] For these reasons, more efficient, stable and less costly materials for the iodine capture in gas phase are required. In this line of thought, numerous researches were devoted to the design of new thermally stable nanoporous materials, such as aluminium-[6, 7] or alkali-[8] zeolites, zeolite-related structures ("zeoballs")[9] or Metal-Organic-Frameworks (MOFs)[10-14] able to selectively and efficiently capture $I_2$ in gas and liquid phases. Recently, we also demonstrated that the thermally stable and porous cyano-bridged coordination polymer called Hofmann-type clathrate having the formula $Ni^{II}(pz)[Ni^{II}(CN)_4]$ (where pz = pyrazine) presents a high affinity to the iodine capture due to a selective insertion of $I_2$ into the cavities of the crystalline network through the formation of weak interactions with pyrazine and cyanometallate. This compound is able to reversibly capture the iodine in both, liquid and gas phases, with a maximal capacity of 1 mole of $I_2$ per mole of Hofmann-type structure, which is higher or comparable to other efficient nanoporous materials.[15]

However, the direct use of bulk coordination polymers as a microcrystalline powder in decontamination processes presents several drawbacks due to the instability under irradiation, the difficulty of management and storage of the ultimate radioactive wastes. In order to avoid these problems, the synthesis of nanocomposites based on coordination polymer nanoparticles inserted into appropriated porous matrices seems to be a promising approach. In this line of thought, nanocomposite materials containing Prussian Blue type nanoparticles of 3 – 6 nm that were grown directly within mesoporous silica or porous glass pearls were recently proposed for the selective and effective $Cs^+$ absorption in a column process.[16 - 19] In this system, a good control of the nanoparticles' composition, nanoparticles' size and nanoparticles' quantity inserted into the silica was obtained. The nanocomposites not only absorb cesium ions more efficiently in comparison with the bulk materials (per gram of the Prussian Blue), but also permit the implementation of the decontamination in a column process.

The present manuscript describes the synthesis and characterization of mesoporous silica- and porous glass pearls- based nanocomposites containing covalently linked nanoparticles of Hofmann-type structure $Ni^{II}(pz)[Ni^{II}(CN)_4]$ inside the pores and their use as

efficient sorbent of molecular iodine. The choice of these matrices is explained by the high mesoporosity of silica, as well as by the possibility of easy anchoring of various functional groups to the silica walls. For these reasons, mesostructured silica can be used as a model matrix for the nanocomposites prepared in this study. On the other hand, even if porous glasses have lower surface area than silica, they present better thermal and chemical stability, higher mechanical hardness and greater resistance to damages caused by irradiation.[20] In addition, they are compatible with current radioactive wastes management.[21] The Hofmann-type structure at the nanoscale was chosen due to its high affinity to the molecular iodine and its high efficiency for $I_2$ retention (1 molecule of $I_2$ per unit cell), its relatively high thermal stability (400 °C), the possibility of reversible iodine capture and simplicity of synthesis at room temperature. It should be noted that the synthesis of nanoparticles of analogue structures as $Fe^{II}(pz)[Pt^{II}(CN)_4]$ was previously reported inside the chitosan beads[22] or by a reverse micelles methods,[23] but so far none tried the preparation of mesoporous silica- and porous glass pearls- based nanocomposites. In this work, the $Ni^{II}(pz)[Ni^{II}(CN)_4]$ nanoparticles are covalently anchored to the pores walls of the silica-based supports through grafted diamino functionalities avoiding the risk of their leaching during the iodine sorption. Iodine uptake by these nanocomposites is carried out in a liquid cyclohexane phase to investigate the sorption kinetics and isotherms as well as to understand the sorption mechanisms. The iodine sorption capacity of the nanocomposites is also compared with that of the corresponding bulk Hofmann-type structure and the parent functionalized silica matrices. A study on the potential reversibility and cyclability of the iodine capture is also performed.

## Experimental Section

**A. Synthesis.**

All materials were purchased from commercially available sources, and used without further purification. $Ni(BF_4)_2{\cdot}6H_2O$, $(C_4H_9)_4NBr$, $K_2[Ni(CN)_4]$, pyrazine, HCl, TEOS, mesytilene, Pluronic 123, 2-aminoethyl 3-aminopropyl triethyloxisilane were purchased from Alfa Aesar. Iodine, cyclohexane, methanol and toluene were purchased from Sigma-Aldrich. All the reactions were carried out under aerobic conditions using analytical grade solvents. Glass pearls were purchased from Vitrabio®. The synthesis of $(TBA)_2[Ni(CN)_4]$ (TBA = tetrabutylammonium) has been performed by a metathesis reaction as previously published.[24]

**Synthesis of functionalised mesoporous silica (*Sil*) and glass pearls (*Glass*).** For the preparation of the mesoporous silica, the protocol were taken from literature.[25-29] For this, 4.00 g of Pluronic 123 are dissolved in an acidic solution prepared with 8.75 g of HCl in 120 ml of bi-distilled water. Subsequently, the temperature is raised to 35 °C and 6.80 g of mesitylene (1,3,5-trimethyl benzene) are added and stirred for 3 hours. 8.50 g of TEOS are then added to the solution and stirred for 1 hour. A hydrothermal treatment is performed in a 600 ml Teflon autoclave at 100 °C for 24 hours. The obtained gel is filtered and treated at 550 °C for 6 hours under air flux in order to remove the organic traces.[16 - 18] The preparation of commercial glass beads consisted in a pre-treatment at 150 °C overnight under vacuum, in order to activate the OH groups on the surface.

The grafting of mesoporous silica and glass pearls was carried out in inert conditions in order to avoid oxidation of the grafting agent.[29] 2.00 g of the support and 2.00 g of the grafting agent (2-aminoethyl-3-aminopropyl trymethyloxylsilane) are mixed in a large amount (250 ml) of distilled toluene under Ar atmosphere. Reflux conditions are set at 110 °C, for 48 hours. After filtration the materials were washed with toluene and dried at 90 °C.

Elemental analysis:

*Grafted silica (Sil)*: Si, 38.18 %; C, 10.50%; N, 4.11%; H, 2.37% (grafting of 17 wt% organic groups).

*Grafted glass pearls (Glass)*: Si, 41.84%; C, 5.45%; N, 2.16%; H, 1.42% (grafting of 9 wt% organic groups).

**Synthesis of nanocomposites *Sil@NP* and *Glass@NP*.** Nanocomposite materials *Sil@NP* and *Glass@NP* were obtained starting from the grafted supports by cyclic infiltration (5 cycles) of precursors. A cycle consists in mixing 1 g of functionalized matrix (*Sil* or *Glass*) with a methanolic solution of $Ni(BF_4)_2{\cdot}6H_2O$ and pyrazine with concentration $4{\cdot}10^{-2}$ M. for 2 hours; subsequently the material is filtered under vacuum, thoroughly washed with pure methanol and kept in contact for 2 hours with a methanolic solution of $(TBA)_2[Ni(CN)_4]$ (TBA = tetrabutylammonium) with concentration $4{\cdot}10^{-2}$ M. It is very important to wash with pure methanol after each cycle in order to avoid precipitation of the bulk Hofmann-type structure outside the silica pores. After 5 cycles, the silica turns to pink due to the growth of the Hofmann-type structure nanoparticles into the pores.

Elemental analysis:

*Sil@NP*: Si, 29.35 %; Ni, 14.58 %; C, 14.79%; N, 10.76%; H, 2.18%.

*Glass@NP*: Si, 29.47 %; Ni, 7.00 %; C, 9.44%; N, 5.18 %; H, 1.23 %.

**Iodine sorption experiments.** Kinetic experiments of the iodine sorption for the investigated material were performed by detecting the decrease in iodine concentration in cyclohexane with a transmission UV-VIS spectrometer at different times. For this, 20 mg of the investigated materials (*Sil*, *Glass*, *Sil@NP* and *Glass@NP*) were shaken with 20 ml of $3{\cdot}10^{-3}$ M iodine solution in cyclohexane for different period of time up to 60 h.

In order to determine the sorption isotherms, the materials were kept in dynamic contact with different concentrations of iodine *i.e.* $2.6{\cdot}10^{-3}$, $8{\cdot}10^{-3}$, $1.5{\cdot}10^{-2}$, $4{\cdot}10^{-2}$, $7{\cdot}10^{-2}$ M in cyclohexane (iodine solubility limit in cyclohexane is around $8{\cdot}10^{-2}$ M, so that it was not possible to use higher concentrations), at an equilibrium time determined in kinetic experiments (24 h and 48 h, respectively for nanocomposites and functionalized matrices). Experiments were performed with a powder-solution ratio of 1 mg/ml. The amount of iodine absorbed in materials was determined from measuring the residual concentration of iodine in solution by UV-Vis at the end of the experiment. After sorption, the materials were placed in a cartridge in a Soxhlet apparatus and thoroughly washed with cyclohexane for 24 h in order to remove the surface absorbed iodine.

**Cyclability experiments.** Iodine desorption was performed at 250 °C during 4 h under a continuous flux of argon for *Sil@NP* and *Glass@NP* nanocomposites. In order to verify the possible cyclability of the obtained nanocomposites, two sorption/desorption cycles were then achieved. From these experiments, estimation of the amount of desorbed iodine allowed a rough quantification of the free grafting agent that was not covalently bound to the nanoparticles, giving 0.10 $mmol.g^{-1}$ (1 wt%) for *Sil@NP* and 0.3 $mmol.g^{-1}$ (0.3 wt%) for *Glass@NP*.

**B. Characterization methods.**

Thermal analyses were performed with a STA 409 Luxx Instrument under nitrogen flow with a heating rate of 5 °C.min$^{-1}$. Infra Red spectra were recorded on a Perkin Elmer 1600 spectrometer with a 4 cm$^{-1}$ resolution in KBr disks. UV-Vis spectra were recorded on an Analityk Jena Specord 210 spectrometer. Elemental analyses were performed by the Service Central d'Analyse (CNRS, Villeurbanne, France). Nitrogen and carbon content in the samples was determined using LECO instrument. The samples were heated at 3000 °C under oxygen. Nitrogen and carbon were transformed respectively in $NO_x$ and CO and detected by using an IR detector. Iodine content was determined by measuring the residual concentration of iodine in solution using UV-Visible spectroscopy. Powder X-ray diffraction patterns were measured on a Bruker® D8 advanced Diffractometer in Bragg-Bentano geometry with Ni-filtered Cu-Kα radiation. The measurement parameters are: step size 0.02008; counting time 15 sec. Samples for Transmission Electron Microscopy (TEM) measurements were prepared using extractive replicas or ultramicrotomy techniques. Extractive replica technique consists in depositing on a freshly cleaved mica plate a suspension of the nanocomposite in ethanol. After evaporation of the ethanol, a carbon film is deposited onto the mica plate. Then, the latter is immersed in a diluted HF solution. The carbon film is then detached from the mica plate and floats on the surface of the solution which allows dissolving the silica part of the nanocomposite keeping the Hofmann-type clathrate nanoparticles sticking on the carbon film. After washing twice the carbon film, it is deposited onto copper grids for TEM observations. Thus, this technique allows visualizing the Hofmann-type structure nanoparticles after the removal of silica. Ultramicrotomy technique consists in suspending the material in a resin which is polymerized at low temperature (*i.e.* 70 °C), then slices of *ca.* 60 to 100 nm are cut with an ultramicrotome apparatus equipped with a diamond knife. This technique allows visualizing especially silica matrix because the slow difference of the electronic density between the matrix and nanoparticles. TEM measurements were carried out at 100kV with a microscope JEOL 1200 EXII. The nanoparticles' size distribution histograms were determined using enlarged TEM micrographs taken at magnification of x50K. A large number of nanoparticles were counted in order to obtain a size distribution with good statistics. Scanning Electron Microscopy measurements were performed with a Philips Quant 200 operating at 15 kV equipped with a Bruker detector. System software for EDX analysis was developed by Bruker. Surface area was obtained using nitrogen adsorption isotherms on an ASAP2020 analyser from Micromeritics. Samples were outgassed under vacuum at 60 °C over night prior to analysis. Surface area was determined using Brunauer – Emmet – Teller (BET) method.

## Results and Discussion

### A. Synthesis and characterisations of silica-based nanocomposites containing Hofmann-type structure $Ni^{II}(pz)[Ni^{II}(CN)_4]$ nanoparticles.

The synthesis of the hybrid nanocomposites supporting $Ni^{II}(pz)[Ni^{II}(CN)_4]$ Hofmann-type structure nanoparticles confined into both, mesoporous silica or porous glass pearls was performed by a multistep approach consisting on the successive coordination of the molecular precursors to the functionalized silica matrix (porous silica or glass pearls) (Fig. 1 and Fig. S1, SI).

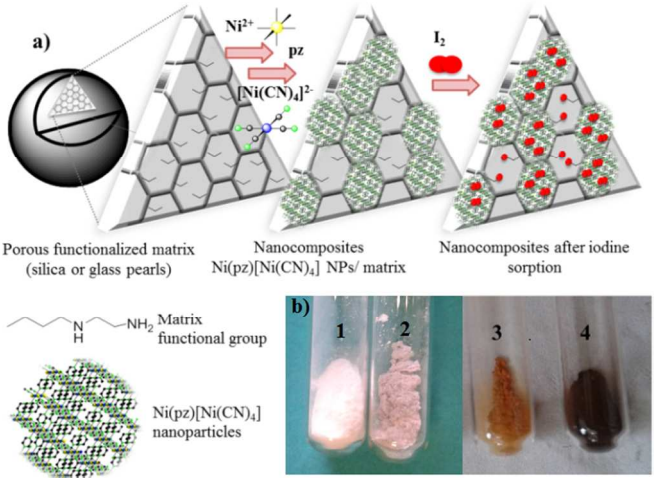


**Fig. 1.** a) Schematic representation of the used approach for the synthesis of silica based nanocomposites containing Hofmann-type structure nanoparticles and their employment for the iodine capture; b) Photographs of the: (1) functionalised silica (*Sil*), (2) silica based nanocomposite *Sil@NP*, (3) functionalised silica (*Sil*) after iodine capture, (4) silica based nanocomposite *Sil@NP* after iodine capture.

At the first step, the mesoporous silica and glass pearls were functionalized with the diamine functionality (matrix functional group in Fig. 1).[30] Diamine-grafted mesoporous silica (*Sil*) was prepared as described in the Experimental section. Its preparation differs from the typical SBA-15[27, 28] synthesis due to the mesytilene use that allows achieving an open and disordered porous network with larger pores, as can be seen by the Transmission Electronic Microscopy (TEM) image shown in Fig. 2a. Thermogravimetric analysis (TGA) indicates the grafting of 16 wt% of the (2-aminoethyl)-3-aminopropyl functionality to the silica walls (Fig S2-a, SI). The closed amount of grafted organic groups (17%) was also confirmed by elemental analyses (see Experimental section). The $N_2$ adsorption isotherms performed at 77 K were analyzed with the BET (Brunauer-Emmett-Teller) method to find the specific surface area and with the BJH (Barrett-Joyner-Halenda) method to determine the pore distribution. The isotherms and pore distributions of the silica before and after grafting are shown in Fig. 3. Porous silica initially shows a specific surface of 646 cm$^2$.g$^{-1}$ with an average pore dimension of 9 nm. As expected, a decrease of the specific surface to 270 cm$^2$.g$^{-1}$ with an average pore size of 7 nm is observed after anchoring of the organic functionalities (Fig 3).
Porous glass pearls coming from Vitrabio® with a pore size of approximately 40 nm (Fig. 2b) having specific area of 130 cm$^2$g$^{-1}$ (Fig. S3, SI) and grain sizes from 200 to 500 µm were also considered as a matrix to prepare the nanocomposites. The preparation of the diamine-grafted glass beads (*Glass*) by the (2-aminoethyl)-3-aminopropyl functionality was performed by using the same procedure than in the case of the silica matrix and described in the Experimental section. TGA and elemental analyses performed for *Glass* sample indicate an anchoring of 9 wt% of organic moieties. That means that, expressed as grams per unit surface, a grafting of $6.9 \cdot 10^{-4}$ g/m$^2$ was carried out on *Glass*. This value is higher than the one of $2.4 \cdot 10^{-4}$ g/m$^2$ obtained for *Sil*. *Glass* sample exhibits a decrease of the specific surface to 83 cm$^2$.g$^{-1}$ and the pores size to 30 nm.

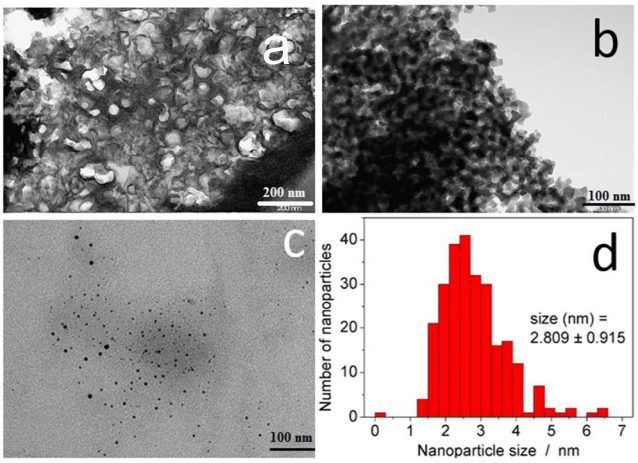


**Fig. 2.** TEM images of a) functionalized mesoporous silica (*Sil*); b) functionalized glass pearls (*Glass*); c) Hofmann-type $Ni^{II}(pz)[Ni^{II}(CN)_4]$ nanoparticles after extractive replicas on *Sil@NP*; d) size distribution for $Ni^{II}(pz)[Ni^{II}(CN)_4]$ nanoparticles from *Sil@NP*.

The second step of the used strategy (Fig. 1) consists in the intrapore growth of the $Ni^{II}(pz)[Ni^{II}(CN)_4]$ nanoparticles by adapting a previously described step-by-step procedure for Prussian Blue analogues.[16-18, 31, 32] For this, functionalized matrices (*Sil* and *Glass*) were shaken first in a $4{\cdot}10^{-2}$ M methanolic solution of $Ni(BF_4)_2{\cdot}6H_2O$ and pyrazine for 2 h. Then the solid is filtered, thoroughly washed with methanol and shaken with a $4{\cdot}10^{-2}$ M methanolic solution of $(TBA)_2[Ni(CN)_4]$ (TBA = tetrabutylammonium) for 2 h. This procedure was repeated 4 more times and the color of the matrices turns to pink due to the growth of the Hofmann-type nanoparticles inside the pores (Fig. 1 and S1). The elemental analysis on the final nanocomposite *Sil@NP* indicates a weight ratio Ni/Si = 0.55 (molar ratio Ni/Si = 0.28) meaning a loading of 39 wt% of nanoparticles into the silica pores. For *Glass@NP*, a weight ratio of Ni/Si = 0.24 (molar ratio Ni/Si = 0.11) corresponds to the presence of 18 wt% of Hofmann-type nanoparticles, that is in accordance to the lower quantity of grafted organic functionalities in glass. Indeed, even though the amount of organic functionalities grafted per unit surface on the glass matrix is higher than the silica one, the significantly higher specific surface area of the latter leads to a higher final content of organic moieties per gram of material and thus to a higher content of the Hofmann-type structure nanoparticles. It is estimated that around 1.1 wt% and 0.3 wt% of grafted amines are not coordinated with nanoparticles on Sil@NP and Glass@NP, respectively (Table 1 and Experimental section).

For both nanocomposites, TGA curves show a two-steps decomposition profile with first the organic functionalities decomposition at 250 °C and second the Hofmann-type structure nanoparticles decomposition at 300 °C. The two steps decomposition is better distinguished for the glass-based nanocomposite (Figs. S2-a and S2-b, ESI). Note that a lower decomposition temperature observed for nanoparticles with respect to the one of the $Ni^{II}(pz)[Ni^{II}(CN)_4]$ bulk materials (400 °C) can be associated with the smaller grain size and the higher surface energy.[33] The specific surface area of nanocomposites *Sil@NP* and *Glass@NP* was determined by the BET method on the nitrogen isotherms at 77 K. As expected, a decrease of the specific surface to 37 $cm^2.g^{-1}$ for *Sil@NP* and to 66 $cm^2.g^{-1}$ for *Glass@NP* in comparison to the corresponding nanoparticles-free functionalized matrices (*Sil* and *Glass*, respectively) is observed and assigned to the filling of the pores with the nanoparticles (Table 2, Figs. 3 & S3, SI).

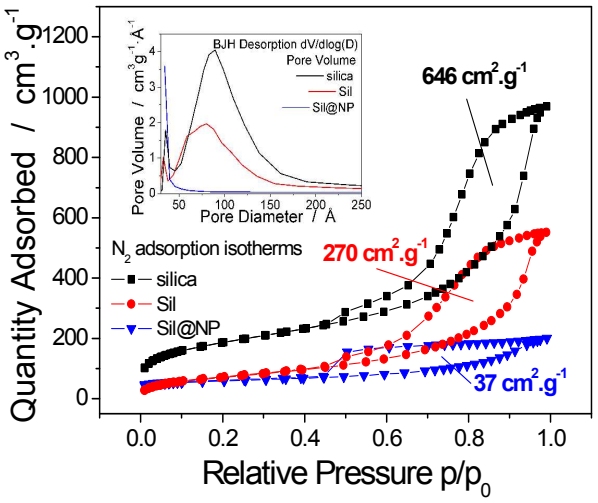


**Fig. 3.** Nitrogen adsorption isotherms at 77 K for the mesoporous silicas before, after diamine groups grafting (*Sil*) and silica based nanocomposite *Sil@NP*. Inset: pore size distribution for the mesoporous silicas before, after diamine groups grafting (*Sil*) and nanocomposite *Sil@NP*.

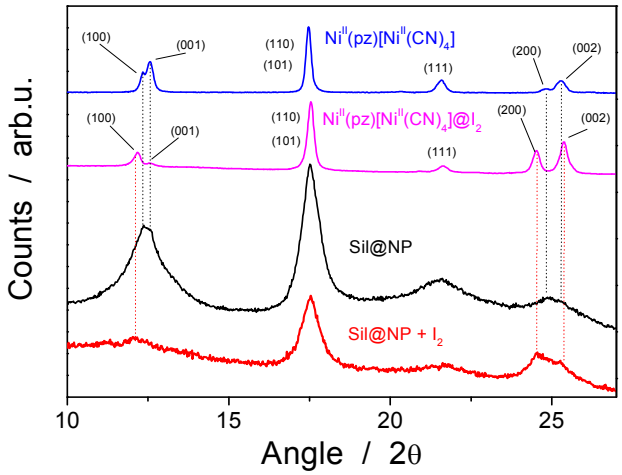


**Fig. 4.** X-Ray powder diffraction (XRPD) patterns for *Sil@NP* nanocomposite and the bulk $Ni^{II}(pz)[Ni^{II}(CN)_4]$ before and after iodine uptake.

The presence of the nanoparticles in the matrix pores of *Sil@NP* was confirmed by X-Ray powder diffraction (XRPD), where the diffraction pattern of $Ni^{II}(pz)[Ni^{II}(CN)_4]$ (tetragonal $P_4/m$ space group)[34] is clearly recognized by comparison with the XRPD pattern of the bulk material (Fig. 4). Solid state UV-VIS spectra in reflectance mode also indicated an absorption band at 550 nm for *Sil@NP* and *Glass@NP*, respectively, matching with the *d-d* transitions in the spectrum of the bulk Hofmann-type structure (Table 1, Insert of Fig. 5, Fig. S4, SI). In addition, Infrared spectra of both samples show the cyanide vibration ν(C≡N) at 2172 $cm^{-1}$, characteristic of the bridging coordinated cyanides in the parent bulk Hofmann-type structure (Table 2, Fig. S5, SI).[15, 34] Direct

observation of the nanoparticles by TEM was possible only for *Sil@NP* by using the HF etching procedure devoted to dissolving of the silica matrix (see Experimental Section). The representative images show the presence of spherical in shape and non-aggregated nanoparticles with a mean size distribution of 2.8 ± 0.9 nm (Fig. 2 c-d). All these results are in accordance with the successful growth of the small Hofmann-type nanoparticles into the pores of both matrices.

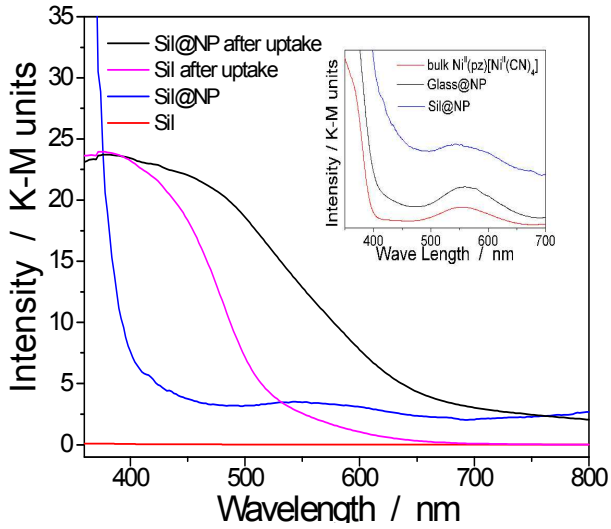


**Fig. 5.** UV-VIS spectra in solid state performed for the grafted silica *Sil*, *Sil@NP* nanocomposite and the bulk $Ni^{II}(pz)[Ni^{II}(CN)_4]$ before and after iodine uptake. Inset: Magnification of UV-VIS spectra in the 350 – 700 nm range for *Sil@NP*, *Glass@NP* nanocomposites and bulk $Ni^{II}(pz)[Ni^{II}(CN)_4]$.

**Iodine capture.**

The nanocomposites *Sil@NP* and *Glass@NP* were employed for the entrapment of iodine in cyclohexane solutions. The iodine sorption in cyclohexane was used as a model for the iodine sorption by the nanocomposites because the iodine concentration may be easily controlled and detected by UV-Vis spectroscopy.[6, 35] The relative diamine-grafted supports without nanoparticles (*Sil* and *Glass*) were also tested in order to evaluate the role of the (2-aminoethyl)-3-aminopropyl functionality to the iodine capture. A thermal activation of the samples was performed at 80 °C under primary vacuum during 8 h in order to remove the interstitial solvent molecules before the iodine uptake. Kinetic studies were performed first at an iodine concentration of $3 \cdot 10^{-3}$ M in order to determine the equilibrium time and the reaction order. For these experiments, 20 mg of the materials were shaken with 20 ml of the iodine solution in cyclohexane for different period of time up to 60 h and the residual concentration of iodine in solution was measured by using UV-VIS electronic spectroscopy. All kinetic curves were fitted with a pseudo-second order model (Fig. 6), which is described by the formula:

$$Q = \frac{kQ_e t}{1+kQ_e^2 t},$$

where Q ($mmol.g^{-1}$) is the amount of entrapped iodine at time t (min), $Q_e$ is the entrapped amount at equilibrium ($t \rightarrow \infty$) and k ($g \cdot mmol^{-1} min^{-1}$) is the kinetic constant. The $I_2$ sorption kinetic curves show that the process is quite rapid for the bulk $Ni^{II}(pz)[Ni^{II}(CN)_4]$ with the equilibrium reached after 2 h (Fig. 6).[13] The equilibrium time for *Sil@NP* and *Glass@NP* samples is equal to around 14 h, whereas the process is much longer for the nanoparticles-free samples *Sil* and *Glass* (48h) (Figs. 6 & S6, SI).

For a complete characterization of the iodine uptake by these materials, sorption isotherms were obtained by iodine capture in solution of cyclohexane at increasing iodine concentrations. The isotherm curves were fitted with the Langmuir model, which is described by the following formula:

$$\frac{Q_e}{Q_{max}} = \frac{KC}{1+KC},$$

where $Q_e$ ($mmol.g^{-1}$) is the amount of entrapped iodine at equilibrium concentration C ($mol.L^{-1}$), $Q_{max}$ ($mmol.g^{-1}$) is the maximal capacity of the material and K is the adsorption energy ($l.mol^{-1}$). Curves and related fittings with the Langmuir model are reported in Fig. 7 for mesoporous silica-based materials and in Fig. S7 (SI) for the glass pearls–based materials. All isotherms present a concave trend with a steep increase at low concentration indicating a good affinity for iodine.

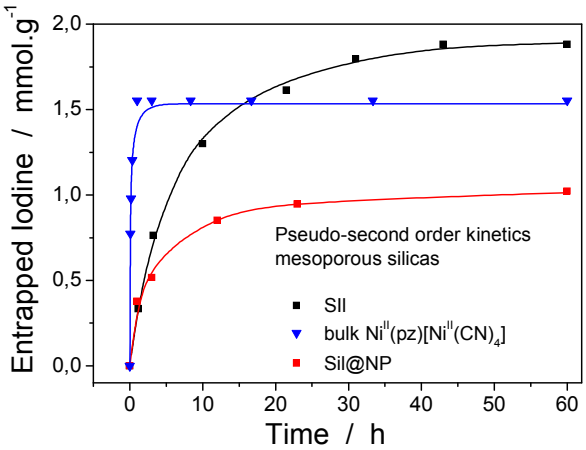


**Fig. 6.** Kinetic curves for the grafted silica, the *Sil@NP* nanocomposite and the bulk $Ni^{II}(pz)[Ni^{II}(CN)_4]$ material in a cyclohexene solution. The solid lines represent the fit with a pseudo-second order model.

Firstly, both grafted matrices are able to capture the iodine from solution due to the presence of the diamines groups. The maximal sorption capacity of 4.1 ± 0.1 $mmol.g^{-1}$ (99 wt%) for *Sil* and of 2.1 ± 0.1 $mmol.g^{-1}$ (53 wt%) for *Glass* were found (Table 1). The smaller amount of absorbed iodine by glass matrix in comparison with the silica is explained by smaller quantity of grafted diamino functionality (17 wt% for *Sil* and 9 wt% for *Glass,* respectively).

Secondly, the nanocomposite materials show maximal absorption capacities equal to 1.7 ± 0.1 $mmol.g^{-1}$ (46 wt%) for *Sil@NP* and 1.1 ± 0.1 $mmol.g^{-1}$ (28 wt%) for *Glass@NP* (Table 2). This apparently lower capacity in comparison with the one of the bulk Hofmann-type structure (3.28 $mmol.g^{-1}$) is explained by the fact that the nanocomposites contain only 39 and 18 wt% of $Ni^{II}(pz)[Ni^{II}(CN)_4]$ in *Sil* and *Glass* matrices, respectively. Neglecting the iodine captured by residual

**Table 1. Some characteristics of nanocomposites *Sil@NP* and *Glass@NP* and their related functionalized matrices.**

*calculated from iodine desorption experiments

| Samples | SSA, $cm^2.g^{-1}$ | Free diamine functionality, wt % | NPs loading, wt % | $t_{eq}$, h | $Q_{max}$, $mmol.g^{-1}$ | $Q_{max}$, wt % |
|---|---|---|---|---|---|---|
| $Ni(pz)[Ni(CN)_4]$ | | - | - | 2 | 3.28 | |
| *Sil* | 270 | 17 | - | 48 | 4.01 (on free diamines) | 99 (on free diamines) |
| *Sil@NP* | 37 | 1.1 (residual) | 39 | 14 | 1.75 (1.49 on NPs and 0.25 on residual diamines*) | 46 (39.1 on NPs and 6.9 on residual diamines) |
| *Glass* | 83 | 9 | - | 48 | 2.10 (on free diamines) | 53 (on free diamines) |
| *Glass@NP* | 66 | 0.3 (residual) | 18 | 14 | 1.10 (1.01 on NPs and 0.07 on residual diamines*) | 28 (25.7 on NPs and 2.3 on residual diamines) |

diamines (see after), iodine sorption capacity of the nanocomposites were recalculated in mmol per gram of inserted Hofmann clathrate giving the capacity of 3.77 and 5.96 $mmol.g^{-1}$ of clathrate for *Sil@NP* and *Glass@NP*, respectively. In both cases, the iodine uptake by clathrate nanoparticles is higher in comparison with the one obtained for the bulk analogous (3.28 $mmol.g^{-1}$; one molecule of $I_2$ per unit cell) demonstrating that the higher efficiency of the nanoparticles in comparison with the corresponding bulk material, which is due to the higher available surface of the nanoparticles for physisorption.

In order to understand the iodine capture mechanism, investigated materials with maximal iodine loading were characterized. First of all, the nanoparticles-free functionalized matrices (*Sil* and *Glass*) were investigated. Both matrices present similar feature over the iodine capture characteristic of the triiodide ($I_3^-$) formed through the strong charge transfer occurring between the iodine and the σ-electron donor diamine functionality.[36-38] Note also that the formation of an additional pentaiodide ($I_5^-$) species was observed for the glass pearls as a result of the interactions between $I_2$ and $I_3^-$,[39-41] but pentaiodide formation was not observed in silica. Indeed, Raman spectrum of *Sil* sample performed in the range 50 – 300 $cm^{-1}$ shows a large peak at 150 $cm^{-1}$ and a peak at 103 $cm^{-1}$ classically assigned to the symmetric and the asymmetric stretching of $I_3^-$ (Fig. 8, Table 2).[41, 42] In contrast, the spectrum of *Glass* sample shows three bands related to $I_5^-$ species: two band for $I_3^-$ (at 110 and 150 $cm^{-1}$) and an additional band at 160 $cm^{-1}$ for interacting $I_2$ (Fig. 8, Table 2).[41, 42] This conclusion is also confirmed by the solid state UV-VIS spectra in diffuse reflectance mode showing a maximal absorption band at

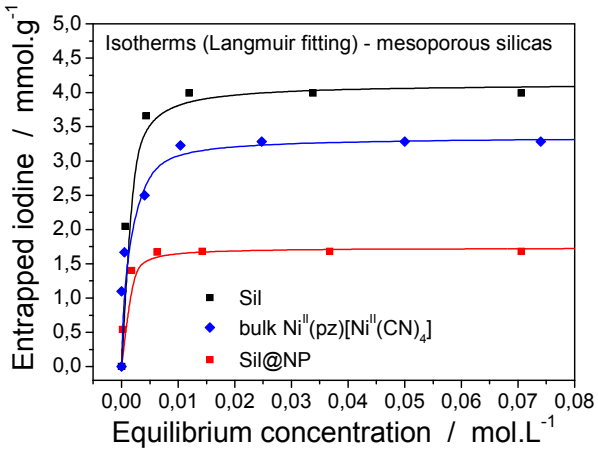


**Fig. 7.** Iodine absorption isotherms in a cyclohexane solution for the grafted silica, the *Sil@NP* nanocomposite and the bulk $Ni^{II}(pz)[Ni^{II}(CN)_4]$ material. The solid lines represent the fit with the Langmuir model.

360 nm for the $I_3^-$ species, characteristic of the large HOMO and LUMO separation for the iodine molecule occurring during the charge transfer in *Sil* (Table 2, Figs. 5 and S5, SI).[43] But when iodine is confined in grafted glass pearls, two bands at 360 nm ($I_3^-$) and at 450 nm (interacted $I_2$) are visible in the spectrum (Table 2, Fig. S4, SI). This fact explains the yellow color of *Sil* and the red one of *Glass* sample observed after the iodine capture (Fig. 1). Therefore, as described in literature,[44] when iodine interacts with σ-electron donors, such as the diamine functionality grafted to the silica wall, a strong charge transfer occurs. The σ-electrons are given to the anti-bonding orbital 5σ* of iodine bringing to ionic dissociation:

$$N: + 2\ I_2 \rightarrow N:I^+ + I_3^-$$

where N: is an amino group of the diamine functionality. For this reason, long equilibrium times (48 h) is observed for the nanoparticles-free functionalised silica or glass pearls samples, which is explained by creation of new chemical bonds; a chemisorption mechanism may be assumed. On the other hand, the presence of the pentaiodide species for glass pearls may be justified by the activation of the later before the diamine grafting, which increases the number of $OH^-$ groups per unit surface leading not only to a higher density of grafting agents per unit surface but also to the formation of the stable $I_3^-/I_5^-$ entities like interactions of iodine with ethanol molecules.[42] A theoretical maximal capacity for both nanoparticles-free materials is 4 moles of iodine per mole of diamine. Considering this, the amount of entrapped iodine of 4.1 $mmol.g^{-1}$ and 2.1 $mmol.g^{-1}$ (Table 1) is lower than the expected values of 6.7 $mmol.g^{-1}$ and 3.5 $mmol.g^{-1}$ for respectively functionalized silica and glass pearls. The experimental $I_2$/diamine ratio after iodine loading is indeed found equal to 2.5 for *Sil* and 2.3 for *Glass* instead of 4.

Nanocomposite materials *Sil@NP* and *Glass@NP* obtained after growth of the $Ni^{II}(pz)[Ni^{II}(CN)_4]$ nanoparticles inside the pores of the functionalized matrices show different behaviour regarding the iodine uptake due to the presence of the nanoparticles. Previously, we demonstrate that the physisorption of iodine by the bulk Hofmann-type structure $Ni^{II}(pz)[Ni^{II}(CN)_4]$ is mainly due to the insertion of $I_2$ molecules within the network cages through synergetic interactions with both, the pyrazine pillar ligand and the cyanometallate moieties. A small amount of pentaiodides may also be present due to few lattice defects in the Hofmann-type network.[15] When nanoparticles are introduced in the matrix pores both, the nanoparticles and the residual free diammine functionalities not coordinated to the nanoparticles are involved in the iodine trapping. This hypothesis is supported by the spectroscopic measurements of the nanocomposites after the iodine loading. Raman spectrum of *Sil@NP* shows, in addition to the peaks at 110 $cm^{-1}$ and 150 $cm^{-1}$ associated to $I_3^-$ stretching vibrations observed for *Sil* matrix, an additional peak around 165 $cm^{-1}$ assigned to the presence of confined solid state iodine ($I_2$) found in the spectrum of

the iodine loaded within the bulk Hofmann-type structure (Fig. 8, Table 2).[15] Similarly, the peaks of the glass matrix (110, 150, 160 $cm^{-1}$), as well as the one of the Hofmann-type structure (larger band at 165 $cm^{-1}$) may be observed in the spectrum of *Glass@NP* (Fig. 8, Table 2). Moreover, IR spectra of both nanocomposites after iodine uptake indicate a shift of the cyanide stretching vibration from 2172 to 2167 $cm^{-1}$, which is indicative of an increase in the back-donation d-π* caused by an interaction between the iodine and the tetracyanonickelate moiety observed for the bulk Hofmann-type structure (Fig. S5, SI).[15] Appearance of the band in the 500-520 nm range in UV-VIS spectra of the nanocomposites, characteristic of the confined $I_2$ inside the pores of the Hofmann-type structure nanoparticles confirms this feature (Figs. 5 & S4, SI). XRPD for *Sil@NP* after uptake is in according with modifications as previously described for the bulk phase $Ni^{II}(pz)[Ni^{II}(CN)_4]\bullet I_2$, since the iodine insertion triggers an increase of the lattice parameters: relevantly, the peak at 25° for the Miller plane (200) shifts to lower 2θ values and it increases its intensity with respect to the plane (002) (Fig. 4). [15]

The iodine absorption kinetics curves also indirectly translate the presence of both, the physisorption and the chemisorption mechanisms giving rise to an intermediate equilibrium time observed for nanocomposite materials: the presence of the Hofmann-type structure nanoparticles seems to speed up the iodine uptake.

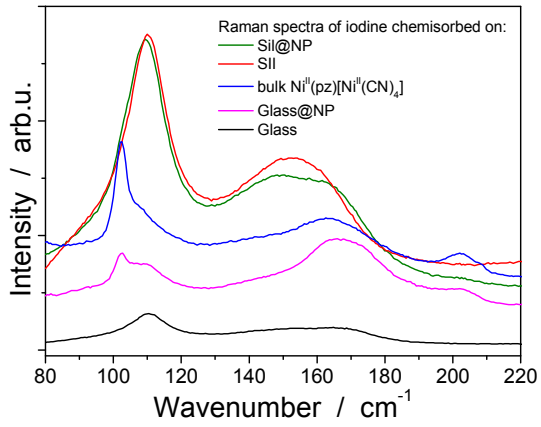


**Fig. 8.** RAMAN spectra in the range 80-220 $cm^{-1}$ for functionalized matrices (*Sil*, *Glass*), bulk $Ni^{II}(pz)[Ni^{II}(CN)_4]$ and nanocomposites (*Sil@NP*, *Glass@NP*) after $I_2$ loading.

**Table 2. Spectroscopic characteristics of the investigated materials before and after maximal iodine capture.**

| Samples after iodine capture | Raman, $cm^{-1}$ | UV-VIS, nm |
|---|---|---|
| $Ni(pz)[Ni(CN)_4]$ | 103 ($I_3^-$ on defects)<br>165 (confined $I_2$) | 550 (clathrate) |
| Sil | 110, 150 ($I_3^-$) | 360 ($I_3^-$) |
| Sil@NP | 110, 150 ($I_3^-$),<br>165 (confined $I_2$) | 360 ($I_3^-$),<br>500 (confined $I_2$)<br>550 (clathrate) |
| Glass | 110, 150 ($I_3^-$),<br>160 ($I_2$ in $I_5^-$ complex) | 360 ($I_3^-$), 450 ($I_2$ in $I_5^-$ complex) |
| Glass@NP | 110, 150 ($I_3^-$),<br>160 ($I_2$ in $I_5^-$ complex),<br>165 (clathrate confined $I_2$) | 360 ($I_3^-$), 450 ($I_2$ in $I_5^-$ complex),<br>520 (clathrate confined $I_2$)<br>550 (clathrate) |

**Cycling ability of iodine sorption.**

As previously shown,[15] a full regeneration of the bulk Hofmann-type structure $Ni^{II}(pz)[Ni^{II}(CN)_4]$ after iodine capture can be performed by its heating at 300 °C during 2 h and three iodine sorption/desorpion cycles were therefore performed.[13]

However, as previously mentioned, nanoparticles show lower thermal stability in comparison with the bulk analogous. For this reason, the iodine desorption executed at 250 °C during 4 h under a continuous flux of argon for the nanocomposites were investigated. The nanocomposite integrity after heating was confirmed by spectroscopy measurements as well as by EDX analyses. The obtained atomic ratio I/Ni = 0.20 for *Sil@NP* means that 1.49 $mmol.g^{-1}$ of $I_2$ was desorbed off and 0.25 $mmol.g^{-1}$ of iodine is still chemisorbed on residual free diamines into the pores. Similarly, *Glass@NP* sample shows an atomic ratio I/Ni equal to 0.12 indicating desorption of 1.03 $mmol.g^{-1}$ of iodine and retaining of 0.07 $mmol.g^{-1}$ after thermal treatment. FT-IR spectra for both nanocomposites show that the ν (C≡N) band at 2167 $cm^{-1}$ was back to the original value of 2172 $cm^{-1}$ meaning that confined iodine was fully evacuated off the nanoparticle's clathrate (Fig. S8, SI), as already demonstrated in our previous work for the bulk material.[15] In addition, a complete vanishing of the band in the range 500 – 520 nm in UV – VIS spectra associated with the presence of the confined $I_2$ is observed. However, the characteristic bands for the presence of residual $I_3^-$ and $I_5^-$ species, respectively for *Sil@NP* and *Glass@NP*, are still observed in the spectra of these desorbed samples (Figs. 9 & S9, SI). This result indicates that the heating of the nanocomposites at 250 °C permits the selective desorption of the iodine confined in the Hofmann-type structure nanoparticles, but the materials retain a small quantity of polyiodides at the residual diamines functionalities. These moieties are lost simultaneously with the decomposition of the organic groups when heating to higher temperature (Fig. S8, SI).

Finally, in order to verify the possible cycling ability of the obtained nanocomposites, two sorption/desorption cycles were achieved indicating a perfect reproducibility of the iodine uptake. Note that UV-VIS spectroscopy newly shows an appearance and then a disappearance of the band at 500 - 520 nm associated with the presence of the confined $I_2$ during the second iodine loading/desorption cycle (Figs. 9 & S9, SI). Contrarily, the iodine sorption on functionalized support is not reversible and the departure of the iodine with heating is occurring with the simultaneous decomposition of the organic anchors.

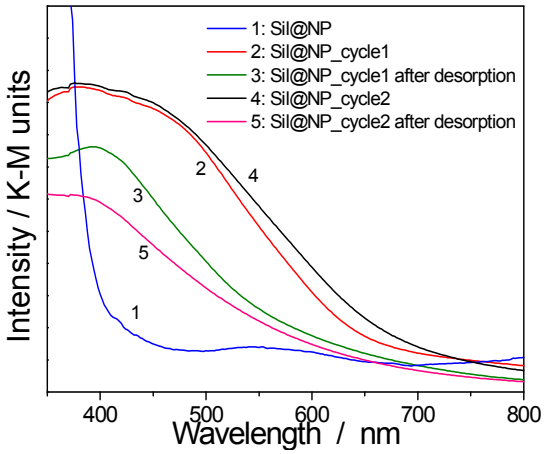


**Fig. 9.** Solid state UV-VIS spectra in diffuse reflectance mode for the cycling process of Sil@NP (2 cycles of iodine uptake and desorption).

## Conclusions

In the present work, we synthesized for the first time two nanocomposites based on Hofmann-type structure nanoparticles $Ni^{II}(pz)[Ni^{II}(CN)_4]$ grown directly into the pores of the mesostructured silica and the porous glass pearls. These materials were obtained by successive coordination of nickel salts, pyrazine and cyanonickelate precursors into the pores through the diamine groups functionalizing the silica walls. Small spherical clathrate nanoparticles of 2 – 3 nm were obtained inside the matrix pores and characterized by IR and Raman spectroscopy, UV-VIS spectroscopy, X-Ray diffraction and TEM analysis. The obtained nanocomposites contain 39 and 18 wt% of nanoparticles for silica and glass pearls, respectively.

The as-obtained nanocomposites were employed for iodine capture in cyclohexane solutions and their iodine sorption behavior was compared with the one of the functionalized parent matrix and the corresponding bulk Hofmann-type clathrate.

The first point to note is that the iodine sorption kinetics of the nanocomposites is four times faster compared to the ones of the parent amino functionalized matrices. Indeed, for the latter a strong charge transfer process is arising between iodine and the σ-electron donor diamine functionality, *i.e.* a chemisorptions process leading to the formation of $I_3^-$ and/or $I_5^-$ species. Contrarily, a physisorption process of molecular iodine into the Hofmann-type network cavities takes place for nanocomposites, speeding up the iodine sorption. Still the presence of the residual amino groups in the nanocomposites slows down the equilibrium sorption time when compared to the bulk Hofmann-type structure.

Secondly, both nanocomposite materials present interesting iodine sorption capacity of 1.7 $mmol.g^{-1}$ and of 1.1 $mmol.g^{-1}$, respectively. The iodine capture occurs mostly on the nanoparticles, but a small quantity of iodide is also retained in the pores through formation of adducts with residual diamines. The sorption capacity calculated by $mmol.g^{-1}$ of the Hofmann clathrate nanoparticles is higher in comparison with the capacity of the corresponding bulk Hofmann clathrate highlighting the efficiency of such supported nanoparticles.

Thirdly, thermal treatments at 250 °C show the reversible desorption of the iodine captured by nanoparticles and cycling ability is clearly observed for both nanocomposites.

In summary, the use of nanocomposite materials containing Hofmann-type structure nanoparticles covalently linked into the pores of supported matrices appears to be a promising approach for efficient reversible iodine capture, which opens interesting perspectives in relation to the many possible variations in chemical composition of these materials for iodine decontamination and further wastes storage.

## Acknowledgements

The authors thank the ANR (ANR-AA-RMNP-003-01), University Montpellier 2 and CNRS for financial support. We also thank Mme D. Granier, (PAC Chimie Balard, Montpellier) for XRPD measurements, M. José-Marie Ruiz for the Raman spectra; Mme Veronique Richard and M. Franck Godiard for the preparation of the TEM grids.

## Notes and references

[a] Institut Charles Gerhardt Montpellier, ICGM, UMR 5253 CNRS-UM2-ENSCM-UM1, Chimie Moléculaire et Organisation du Solide, Université Montpellier II, Place E. Bataillon, 34095, Montpellier cedex 5, France.
[b] CEA/DEN/DTCD/SPDE, Laboratoire des Procédés Supercritiques et de Décontamination, *BP 17171, 30207 Bagnols sur Cèze, France.*
[c] Institute of Chemistry, Department of Applied Science and Technology, Politecnico di Torino, Corso Duca degli Abruzzi 24, 10129 Torino, Italy.

Electronic Supplementary Information (ESI) available: Experimental Part (supplementary), Pictures of glass pearls based samples (**Fig. S1**), TGA curves for obtained materials (**Fig. S2),** Nitrogen adsorption isotherms at 77 K (**Fig. S3**), UV-VIS spectra before and after iodine uptake (**Fig. S4**), FT-IR spectra before and after iodine uptake (**Fig. S5**), Kinetic curves for glass-based materials (**Fig. S6),** Iodine absorption isotherms for glass-based materials (**Fig. S7**), FT-IR spectra at sorption/desorption (**Fig. S8**), UV-Vis spectra demonstrating the cycling ability for the Glass@NP nanocomposite (**Fig. S9**).

1 G. Audi, O. Bersillon, J. Blachot, A. H. Wapstra, *Nucl. Phys. A,* 2003, **729**, 3-128.
2 D. R. Haefner, T. J. Tranter, *Report INL/EXT-07-12299*, 2007, Idaho National Laboratory.
3 N. R. Soelberg, T. G. Garn, M. R. Greenhalgh, J. D. Law, R. Jubin, D. M. Strachan, P. K. Thallapally, *Science and Techn. Nucl. Install*., 2013, **13,** ID702496.
4 a) K. W. Chapman, P. J. Chupas, T. M. Nenoff, *J. Am. Chem. Soc.,* 2010, **132**, 8897-8899; b) T. Nenoff, M. A. Rodrigez, N. R. Soelberg, K. W. Chapman, *Microporous and Mesoporous Materials*, 2014, **200**, 297.
5 S. Matsuoka, H. Nakamura, T. Tamura, Takano, T. Y. Ito, *J. Nucl. Science Techn.,* 1984, **21***,* 862-870.
6 C. Falaise, C. Volkringer, J. Facqueur, T. Bousquet, L. Gasnot, T. Loiseau, *Chem. Commun.,* 2013, **49,** 10320-10322.
7 W. Guo, D. Wang, J. Hu, Z. K. Tang, S. Du, *Appl. Phys. Lett.,* 2011, **98**, 043105-043107.
8 E. J. Doskocil, S. V. Bordawekar, B. G. Kaye, R. J. Davis, *J. Phys. Chem. B,* 1999, **103**, 6277-6282..
9 Y. Lin, W. Massa, S. Dehnen, *J. Am. Chem. Soc.,* 2012, **134**, 4497-4500.
10 D. F. Sava, K. W. Chapman, M. A. Rodriguez, J. A; Greathouse, P. S. Crozier, H. Zhao, P. J. Chupas, T. Nenoff, *Chem. Mater.,* 2013, **25**, 2591-2596.
11 J. T. Hughes, D. F. Sava, T. M. Nenoff, A. Navrotsky, *J. Am. Chem. Soc.,* 2013**, 135**, 16256-16259.
12 P. Cui, L. Ren, Z. Chen, H. Hu, B. Zhao, W. Shi, P. Cheng, *Inorg. Chem.,* 2012, **51**, 2303-2310.
13 D. F. Sava, M. A. Rodriguez, K. W. Chapman, P. J. Chupas, J. A. Greathouse, P. S. Crozier, T. M. Nenoff, *J. Am. Chem. Soc.*, 2011, **133**, 12398-12401.
14 P. Horcajada, F. Salles, S. Wuttke, T. Devic, D. Heurtaux, G. Maurin, G., A. Vimont, M. Daturi, O. David, E. Magnier, N. Stock, Y. Filincuck, D. Popov, C. Rieckel, G. Ferey, C., Serre, *J. Am. Chem. Soc.*, 2011, **133**, 17839-17847.



 

15 G. Massasso, J. Long, J. Haines, S. Devautour-Vinot, G. Maurin, A. Grandjean, B. Onida, B. Donnadieu, J. Larionova, C. Guérin, Y. Guari, *Inorg. Chem.,* 2014, **53, 9,** 4269-4271.
16 J. Larionova, J. Long, Y. Guari, G. Massasso, A. Grandjean, Y. Barré, A. Tokarev, J. Causse, patent FD13715, SP52533FG, 2013.
17 R. Turgis, G. Arrachart, C. Delchet, C. Rey, Y. Barré, Y. Pellet-Rostaing, Y. Guari, J. Larionova, A. Grandjean, *Chem. Mater.*, 2013, **25**, 4447-4453.
18 C. Delchet, A. Tokarev, X. Dumail, G. Toquer, Y. Barre, Y. Guari, C. Guerin, J. Larionova, A. Grandjean, *RSC Advances* 2012, **2,** 5707-5716.
19 J. Causse, A. Tokarev, C. Ravaux, M. Moloney, Y. Barré, A. Grandjean, *J. Mater. Chem.* 2014, **2**, 9461-9464.
20 a) S. Dourdain, X. Deschanels, G. Toquer, C. Grygiel, I. Monnet, S. Pellet-Rostaing, A. J. Grandhean, *Nucl. Mater.,* 2012, **427,** 411-414; b) S. Klaumunzer, *Nucl. Instrum. Methods Phys. Res. B*, 2004, **225,** 136-153.
21 a) M. E. Davis, *Nature*, 2002, **417**, 813; b) P. Makowski, X. Deschanels, A. Grandjean, D. Meyer, G. Toquer, F. Goettmann, *New J. Chem.*, 2012, **36**, 531.
22 a) J. Larionova, L. Salmon, Y. Guari, A. Tokarev, K. Molvinger, G. Molnar, A. Bousseksou, *Angew. Chem. Int. Ed.,* 2008, **47**, 8236-8240. b) A. Tokarev, J. Long, Y. Guari, J. Larionova, F. Quinard, F. Agulhon, M. Robitzer, G. Molnar, L. Salmon, A. Bousseksou, *New J. Chem.* 2013, **37,** 3420-3432.
23 Y. Raza, F. Volatron, S. Moldovan, O. Ersen, V. Huc, C. Martini, F. Brisset, A. Gloter, O. Stephan; A. Bousseksou, L. Catala, T. Mallah, *Chem. Comm.,* 2011, 11501-11503.
24 B. Das, R. Carlin, A. Osteryoung, *Inorg. Chem.,* 1989, **28**, 421-426.
25 L. Cao, T. Man, M. Kruk, *Chem. Mater.,* 2009, **21**, 1144-1153.
26 J. S. Beck, K. D. Vartuli, W. J. Roth, M. E. Leonowitz, C. T. Kresge, K. D; Schmitt, C. T. Chu, D. H. Olson, E. W; Sheppard, S. B. McCullen, J. B. Higgins, J. L. Schlenker, *J. Am. Chem. Soc.,* 1992, **114**, 10834-10843.
27 P. Yang, D; Zhao, B. F. Chmelka, G. D. Strucky, *Chem. Mater.*, 1998, **10**, 2033-2036.
28 Z. Dongyuan, Q. Huo, J. Feng, B. F. Chmelka, 1998, **120**, 6024-6036.
29 L. Wang, T. Qi T. Y. Zhang, J. Chu, *Microp. Mesop. Mat.* 2006, **91**, 156-160.
30 T. Sangvanich, V. Sukwarotwat, R. J. Wiacek, R. M. Grudzien, G. E Frywell, R. S. Addleman, C. Timchalk, W. Yantasee, *J. Hazar. Mater.*, 2010, **182**, 225-231.
31 G. Clavel, Y. Guari, J. Larionova, C. Guerin, *New J. Chem.* 2005, **29**, 275-279.
32 B. Folch, Y. Guari, J. Larionova, C. Luna, C. Sangregorio, C. Innocenti, A. Caneschi, C. *Guerin, New J. Chem.,* 2008, **32,** 273-282.
33 R. W., Hutchinson, S. Kleinberg, F. P. Stein*, J. Phys. Chem.,* 1973, **77,** 870-875.
34 (a) C. Bartual-Murgui, L. Salmon, A. Akou, N. A. Ortega-Villar, H. J. Shepherd, M. C. Munoz, G. Molnar, J. A. Real, A. Bousseksou, *Chem. Eur. J.,* 2012, **18**, 507-516. b) V. Niel, J. M. Martinez-Agudo, M. C. Munoz, A. B. Gaspar, J. A. Real, *Inorg. Chem.*, 2001, **40**, 3838-3839.
35 a) W.-W. He, S.-L. Li, G-S. Yang, Y-Q. Lan, Z.-M. Su, Q. Fu, *Chem. Commun.* 2012, **48,** 10001**;** b) Z.-J. Zhang, W. Shi, Z. Niu, H.-H. Li, B. Zhao, P. Gheng, D.-Z. Liao, S.-P. Yan, *Chem. Commun*., 2011, **47**, 6425.
36 P. Deplano, J. R. Ferraro, M. L. Mercuri, E. F. Trogu, *Coord. Chem. Rev.* 1999, **188**, 71-75.
37 S. Moulay, J. R. Ferraro, M. L. Mercuri, E. F. Trogu, *Polym. Eng.*, 2012, **33**, 389-443.
38 M. Chorro, G. Kane, L. Alvarez, J. Cambedouzou, E. Paineau, A. Rossberg, M. Kociak, R. Aznar, S. Pascarelli, P. Launois, J. L. Bantignies, *Carbon*, 2013, **52**, 100-108.
39 S. Kobinata, S. Nagakura, *J. Am. Chem. Soc.,* 1966, **88**, 3905-3909.
40 J. T. Ye, Y. Iwasa, Z. K. Tang, *Phys. Rev. B,* 2011, **83**, 193409.
41 C. Pei, T. Ben, S. Xu, S. Qiu, *J. Mat. Chem.A,* 2014, **2**, 7179-7187.
42 L. Alvarez, J. L. Bantignies, R. Le Parc, R. Aznar, J. L. Sauvagol, A. Merlen, D. Machon, A. San Miguel, *Phys. Rev. B,* 2010, **82**, 205403; (b) P. H. Svensson, L. Kloo, *Chem. Rev.*, 2003, **103**, 1649-1684.
43 A. Benesi, J. H. Hildebrand, *J. Am. Chem. Soc.,* 1949, **71**, 2703-2707.
44 B. Camarota, Y. Goto, S. Inagaki, E. Garrone, B. Onida, *J. Phys. Chem.* 2009, **113**, 20396-20400.

# Abstract

Hybrid nanocomposites based on nanoparticles of the Hofmann-type structure $Ni^{II}(pz)[Ni^{II}(CN)_4]$ (where pz = pyrazine) confined into mesoporous silica or porous glass pearls were synthesised and studied for efficient iodine capture from solution with a maximal sorption capacity of 1.75 mmol per g of materials.